

RESEARCH ARTICLE

# The transition to aeration in turbulent two-phase mixing in stirred vessels

Lyes Kahouadji<sup>1,\*</sup>, Fuyue Liang<sup>1</sup>, Juan P. Valdes<sup>1</sup>, Seungwon Shin<sup>2</sup>, Jalel Chergui<sup>3</sup>, Damir Juric<sup>3,4</sup>, Richard V. Craster<sup>5</sup> and Omar K. Matar<sup>1</sup>

<sup>1</sup>Department of Chemical Engineering, Imperial College London, South Kensington Campus, London SW7 2AZ, UK

<sup>2</sup>Department of Mechanical and System Design Engineering, Hongik University, Seoul 04066, Republic of Korea

<sup>3</sup>Laboratoire Interdisciplinaire des Sciences du Numérique (LISN), Université Paris Saclay, Centre National de la Recherche Scientifique (CNRS), 91400 Orsay, France

<sup>4</sup>Department of Applied Mathematics and Theoretical Physics, University of Cambridge, Centre for Mathematical Sciences, Wilberforce Road, Cambridge CB3 0WA, UK

<sup>5</sup>Department of Mathematics, Imperial College London, South Kensington Campus, London SW7 2AZ, UK

\*Corresponding author. E-mail: [l.kahouadji@imperial.ac.uk](mailto:l.kahouadji@imperial.ac.uk)

**Received:** 19 January 2022; **Revised:** 27 June 2022; **Accepted:** 22 August 2022

**Keywords:** Stirred vessels; Multiphase mixing; Turbulence; Aeration; Fast-moving consumer goods

## Abstract

We consider the mixing dynamics of an air–liquid system driven by the rotation of a pitched blade turbine (PBT) inside an open, cylindrical tank. To examine the flow and interfacial dynamics, we use a highly parallelised implementation of a hybrid front-tracking/level-set method that employs a domain-decomposition parallelisation strategy. Our numerical technique is designed to capture faithfully complex interfacial deformation, and changes of topology, including interface rupture and dispersed phase coalescence. As shown via transient, a three-dimensional (3-D) LES (large eddy simulation) using a Smagorinsky–Lilly turbulence model, the impeller induces the formation of primary vortices that arise in many idealised rotating flows as well as several secondary vortical structures resembling Kelvin–Helmholtz, vortex breakdown, blade tip vortices and end-wall corner vortices. As the rotation rate increases, a transition to ‘aeration’ is observed when the interface reaches the rotating blades leading to the entrainment of air bubbles into the viscous fluid and the creation of a bubbly, rotating, free surface flow. The mechanisms underlying the aeration transition are probed as are the routes leading to it, which are shown to exhibit a strong dependence on flow history.

## Impact Statement

The combination of innovative numerical algorithms in a single numerical framework, able to accurately handle coupled physics in fluid mechanics, such as multiphase interface motion, fluid–structure interaction and turbulence modelling, is essential for predicting complex mixing flow in stirred vessels. Moreover, a robust high-performance computing architecture enables in-depth understanding of previously inaccessible physics for such extreme flow regimes. In the context of aeration due to mixing in a stirred vessel, where the density ratio between the air and the liquid is  $\sim O(10^3)$ , it is crucial to provide an accurate numerical framework able to encompass all the techniques listed above.

## 1. Introduction

Flow mixing inside stirred vessels occurs in a large array of industrial applications and produces complex dynamical structures. These structures, such as those seen in the work of [Batels, Breuer, Wechdler, and Durst \(2020\)](#) for single-phase flow, exert a strong influence on the mixing efficiency. Many fast-moving consumer goods involve the manufacturing of so-called structured products (e.g. foods, creams, detergents), which are mass-produced via complex multiphase mixing processes of several base products, commonly carried out in agitated tanks. Certain processes and applications require rapid mixing to guarantee the targeted end-product properties, but this may lead to undesirable vortex formation and subsequent entrainment of the gas-phase onto the liquid, causing process inefficiencies. In contrast, in other processes such as ice cream manufacturing ([Douglas Goff, 1997](#); [McClements, 2004](#)) or sensitive mixing in bioreactors, the promotion of ‘aeration’ is essential. Thus it is crucial to predict the mixing patterns in stirred vessels leading to the phenomena of aeration, and to demarcate the aeration threshold as a function of relevant system parameters, such as fluid properties, impeller geometry and rotational speed.

Early studies focusing on turbulent rotating flows mainly gravitate towards flow fields emerging between a rotating disk at the base of a cylinder and a free surface ([Spohn, 1991](#); [Spohn, Mory, & Hopfinger, 1993, 1998](#)). These works have covered a wide array of cases from steady, unsteady and axisymmetric to fully three-dimensional, considering flat as well as deformable free surface flows. The deformation of the free surface was explored by [Vatistas \(1990\)](#). The interface shape initially forms an inverted bell, and as the rotation rate increases, the free surface descends to the rotating disk producing a dry region on the disk in the form of a periodic pattern in the azimuthal direction. Several subsequent studies were devoted to the effect of numerous operational parameters such as disk rotational speed and diameter on these flows ([Jansson, Haspang, Jesen, Hersen, & Bohr, 2006](#); [Suzuki, Iima, & Hayase, 2006](#); [Vatistas, Wang, & Lin, 1992](#)). [Piva and Meiburg \(2005\)](#) proposed a first numerical approximation to detect the free surface deflection but this is limited to small deformations. [Kahouadji and Martin Witkowski \(2014\)](#) performed a numerical study that takes into account the axisymmetric interfacial deformation using curvilinear coordinates.

More recently, papers focusing on turbulent mixing have given further emphasis to the motion driven by the impeller. In spite of the added complexity of a bladed impeller, we still expect to see flow regimes reminiscent of the behaviour under rotating disks. [Ciofalo, Brucato, Grisafi, and Torraca \(1996\)](#) performed a 3-D turbulent flow simulation, where the flow equations are in the rotating reference frame of the impeller with the addition of a conventional linear logarithmic ‘wall function’ as in [Lauder and Spalding \(1974\)](#). [Brucato, Ciofalo, Grisafi, and Micale \(1998\)](#) compared alternative computational methods: the first replaced the impeller by suitable boundary conditions, and the second consisted of dividing the computational domain into two concentric and partially overlapping parts; the inner region, containing the impeller, where the flow is simulated in the impeller rotating reference frame, while in the outer region, simulations are conducted in the laboratory reference frame. This technique requires information exchange between the two regions. Since then, there have been numerous numerical studies on agitated vessels, most of which tackle baffled agitated tanks and their inherent shortcomings (e.g. recirculation and dead zones) ([Ameur, Sahel, & Kamla, 2017](#); [Chisti, 2000](#)). Nonetheless, unbaffled stirred tanks can also be a good alternative to overcome the main disadvantages brought by baffled tanks, for instance, in terms of avoiding undesired attrition ([Aloi & Cherry, 1996](#)) and reducing power consumption ([Rao & Kumar, 2007](#)). A few studies have covered the underlying mixing dynamics within an unbaffled stirred vessel ([Busciglio, Grisafi, Scargiali, & Brucato, 2014](#)). Some of them are devoted to the laminar regime ([Guadarrama-Pérez et al., 2020](#); [Lamberto, Alvarez, & Muzzio, 1999](#)) and a few more deal with the turbulence regime ([Glover & Fitzpatrick, 2007](#); [Li, Wang, Feng, & Gu, 2017](#); [Li, Xiang, & Xiang, 2020](#); [Martínez-de Jesús, Ramírez-Muñoz, García-Cortés, & Cota, 2018](#)). For instance, [Li et al. \(2017\)](#) coupled a volume-of-fluid method to a Reynolds stress model to capture the gas–liquid interface and turbulent flow agitated by pitched blade turbines where the interface deflection reached the impeller hub. In addition, a series of studies have explored the deformation of a free surface due to the

impeller rotation. Busciglio, Caputo, and Scargiali (2013) characterised the free surface shape induced by different types of impeller. Following this, Busciglio, Scargiali, Grisafi, and Brucato (2016) studied the periodic instabilities of the free surface, i.e. oscillation amplitudes and frequencies, by investigating the influence of impeller type, clearance and vessel size. Furthermore, Deshpande, Kar, Walker, Pressler, and Su (2017) developed a correlation to describe the surface depth which is applicable over a wide range of flow regimes (with Reynolds numbers in the range  $100\text{--}10^4$ ).

Despite of the work reviewed in the foregoing, most of which addressed the hydrodynamics within an unbaffled stirred vessel, studies involving unsteady, turbulent, and highly deformable free surface flows remain limited, especially when attempting to perform an in-depth analysis on the rich and complex vortical structures accompanying such flows. Furthermore, the phenomenon of aeration has not yet been studied in detail via numerical simulations despite its obvious importance to industrial applications as highlighted above. Aeration involves the development of sufficiently large interfacial deformations that lead to the interaction of the free surface with the rotating impeller. This, in turn, brings about the entrainment and dispersion of the lighter phase into the underlying denser phase; for gas (air)–liquid systems, the dispersed phase corresponds to bubbles (of air).

Our aim in the present paper is to study the intricacies of two-phase mixing flows in a stirred vessel via a standard LES (large eddy simulation) Smagorinsky–Lilly turbulence model coupled with a direct-forcing method for the motion of the impeller (Fadlun, Verzicco, Orlandi, & Mohd-Yusof, 2000; Mohd-Yusof, 1997). Moreover, our numerical framework is formulated in the context of a high-fidelity front-tracking technique for the interface (Shin, Chergui, & Juric, 2017; Shin et al., 2018) which is able to handle complex interfacial deformation, pinchoff and coalescence. Applying this new numerical scheme for stirred vessels, our results elucidate, for the first time, the challenging transition to aeration and its dependence on flow history (e.g. ramping up impulsively from a stationary state versus increasing the impeller rotational speed following the achievement of a steady-state at lower speeds). A crucial metric for mixing-induced aeration that a numerical framework should be capable of furnishing is the gas/air holdup, which corresponds to the relative amount of gas/air held in the liquid phase. We provide results for the temporal variation of the holdup from our simulation data.

The rest of this article is organised as follows. Section 2 describes the configuration, sets out the governing equations and summarises the computational methods. Section 4 presents results for both the laminar and turbulent regimes highlighting the vortical structures occurring in such flows; the mechanisms leading to aeration are described, followed by a discussion of the turbulent aeration regime. Finally, in § 5, concluding remarks are provided, and ideas for future work are outlined.

## 2. Problem formulation

The configuration we consider is shown in figure 1 and consists of a cylindrical vessel of diameter  $T = 8.5$  cm filled with a viscous fluid up to a height  $H = 7$  cm. The fluid in all simulations is taken to be water or glycerine with air above. The impeller consists of a cylindrical shaft of 0.5 cm diameter, a cylindrical hub of 1 cm diameter and 0.9 cm height, and four blades of 2.5 cm length, 1 cm height, 0.2 cm width, and inclined at  $\alpha = 45^\circ$ . The impeller is immersed inside the vessel with clearance  $C = 3.5$  cm from the bottom of the vessel, and rotating at impeller speed  $f$ . The impeller diameter is  $D = 5$  cm giving a ratio of radii between the vessel and the impeller  $T/D = 1.7$ . The characteristic length, velocity and pressure scales are the impeller diameter,  $D$ ,  $fD$  and  $\rho(fD)^2$ , respectively that determine the Reynolds, Froude and Weber numbers given by

$$Re = \frac{\rho f D^2}{\mu_l}, \quad Fr = \frac{f^2 D}{g}, \quad We = \frac{\rho f^2 D^3}{\sigma}. \quad (2.1a\text{--}c)$$

We solve the Navier–Stokes equations, assuming incompressible and immiscible viscous fluids in a 3-D Cartesian domain  $\mathbf{x} = (x, y, z) \in [0, 8.6]^2 \times [0, 13]$  cm:

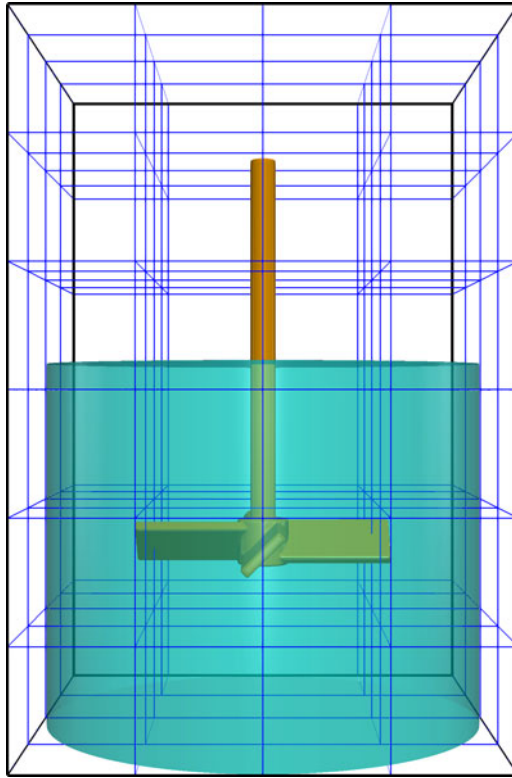


**Figure 1.** Schematic illustration of the computational domain: a stirred vessel defined by an open cylindrical container, partially filled with a viscous liquid, with a pitched-blade turbine immersed within it. The domain is of size 8.6 cm × 8.6 cm × 13 cm and is divided into 4 × 4 × 6 subdomains. The Cartesian structured grid per subdomain is 64<sup>3</sup>, which gives a global structured mesh grid of 256 × 256 × 384.

$$\left. \begin{aligned} \nabla \cdot \bar{\mathbf{u}} &= 0, \\ \rho \left( \frac{\partial \bar{\mathbf{u}}}{\partial t} + \bar{\mathbf{u}} \cdot \nabla \bar{\mathbf{u}} \right) &= -\nabla \bar{p} + \nabla \cdot \left[ (\mu + \rho C_s^2 \Delta^2 |\bar{S}|) (\nabla \bar{\mathbf{u}} + \nabla \bar{\mathbf{u}}^T) \right] + \rho \mathbf{g} + \mathbf{F} + \mathbf{F}_{fsi}. \end{aligned} \right\} \quad (2.2)$$

Equation (2.2), include the Smagorinsky–Lilly LES turbulence model (Smagorinsky, 1963) where  $\bar{\mathbf{u}}$  is the ensemble-averaged fluid velocity ( $\mathbf{u} = \bar{\mathbf{u}} + \mathbf{u}'$ , with  $\mathbf{u}'$  being the turbulent velocity fluctuation),  $t$  the time,  $\bar{p}$  the ensemble-averaged pressure and  $\mathbf{g}$  the gravitational acceleration. Here,  $C_s$  is the well-known Smagorinsky–Lilly coefficient,  $\Delta = V^{1/3}$  where  $V$  is the volume of a grid cell,  $V = \Delta x \Delta y \Delta z$  and  $|\bar{S}| = \sqrt{2\bar{S}_{ij}\bar{S}_{ij}}$  with  $\bar{S}_{ij}$  being the strain rate tensor:

$$\bar{S}_{ij} = \frac{1}{2} \left( \frac{\partial \bar{u}_i}{\partial x_j} + \frac{\partial \bar{u}_j}{\partial x_i} \right) \quad (2.3)$$

(Meyers & Sagaut, 2006; Pope, 2000, 2004). In our study,  $C_s$  is fixed to the value 0.2 as it is quoted in the literature to vary between 0.1 and 0.3 (Deardoff, 1970; Lilly, 1966a, 1966b; Mc Millan & Ferziger, 1979; Pope, 2000). If we set  $C_s = 0$ , (2.2) reduce to the Navier–Stokes equations, without a turbulence model. Here,  $\mathbf{F}$  is the local surface tension force and  $\mathbf{F}_{fsi}$  is the fluid–solid interaction force. We define  $\mathbf{F}$  using a hybrid formulation (Shin et al., 2017, 2018):

$$\mathbf{F} = \kappa_H \nabla \mathcal{H}(\mathbf{x}, t), \quad (2.4)$$

where  $\mathcal{H}$  is an indicator function equal to zero for the gas phase and unity for the liquid phase, respectively. Numerically, this sharp transition is resolved across three to four grid cells with a steep, but smooth, numerical Heaviside function generated using a vector distance function computed directly from the tracked interface (Shin, 2007; Shin & Juric, 2009). In (2.4),  $\kappa_H$  is twice the mean interface curvature field calculated on an Eulerian grid using

$$\kappa_H = \frac{\mathbf{F}_L \cdot \mathbf{G}}{\mathbf{G} \cdot \mathbf{G}}, \quad (2.5)$$

in which  $\mathbf{F}_L$  and  $\mathbf{G}$  are respectively given by

$$\left. \begin{aligned} \mathbf{F}_L &= \int_{\Gamma(t)} \sigma \kappa_f \mathbf{n}_f \delta_f(\mathbf{x} - \mathbf{x}_f) ds \\ \mathbf{G} &= \int_{\Gamma(t)} \mathbf{n}_f \delta_f(\mathbf{x} - \mathbf{x}_f) ds. \end{aligned} \right\} \quad (2.6)$$

In these formulae,  $\sigma$  is the surface tension, assumed constant,  $\mathbf{x}_f$  is a parametrisation of the interface,  $\Gamma(t)$ , and  $\delta_f(\mathbf{x} - \mathbf{x}_f)$  is a Dirac distribution that is non-zero only when  $\mathbf{x} = \mathbf{x}_f$ ,  $\mathbf{n}_f$  is the unit normal vector to the interface and  $ds$  is the length of the interface element;  $\kappa_f$  is twice the mean interface curvature obtained from the Lagrangian interface structure. The geometric information corresponding to the unit normal,  $\mathbf{n}_f$ , and length of the interface element,  $ds$ , in  $\mathbf{G}$  are computed directly from the Lagrangian interface and then distributed onto an Eulerian grid using the discrete delta function. The details follow the well-known immersed boundary approach of Peskin (1977) using our procedure for calculating the force and constructing the function field  $\mathbf{G}$ .

The Lagrangian interface is advected by integrating

$$\frac{d\mathbf{x}_f}{dt} = \mathbf{V}, \quad (2.7)$$

with a second-order Runge–Kutta method where the interface velocity,  $\mathbf{V}$ , is interpolated from the Eulerian velocity. Incorporating the complex geometry of the impeller and its rotation requires the implementation of the so-called direct forcing method (Fadlun et al., 2000; Mohd-Yusof, 1997), which is done by incorporating a fluid–solid interaction force  $\mathbf{F}_{fsi}$  in (2.2). This force is defined numerically using the latest step of the temporal integration of (2.2),

$$\rho \frac{\bar{\mathbf{u}}^{n+1} - \bar{\mathbf{u}}^n}{\Delta t} = \text{local}^n + \mathbf{F}_{fsi}^n, \quad (2.8)$$

where ‘local’ stands for the right-hand-side terms of (2.2) that contain the convective, pressure gradient, viscous, turbulent, gravitational and surface tension force terms. Here, the superscripts denote the discrete temporal step in the computation. In the solid part of the domain corresponding to the impeller,  $\mathbf{F}_{fsi}^n$ , the forced rotational motion  $\mathbf{V}^{n+1}$  is enforced:

$$\bar{\mathbf{u}}^{n+1} = \mathbf{V}^{n+1} = 2\pi f ((y - y_0), -(x - x_0)), \quad (2.9)$$

where  $(x_0, y_0) = (4.3, 4, 3)$  cm is the position of the impeller axis. Hence,  $\mathbf{F}_{fsi}$  is

$$\mathbf{F}_{fsi}^n = \rho \frac{\mathbf{V}^{n+1} - \bar{\mathbf{u}}^n}{\Delta t} - \text{local}^n. \quad (2.10)$$

The no-slip condition is applied for the velocity and the interface on the surface of the impeller parts except for the shaft where we impose a solid rotating motion and axial free-slip condition  $\partial \mathbf{u} / \partial z = 0$ , otherwise, the interface will remain attached to the shaft.

The computational domain (see [figure 1](#)) is a rectangular parallelepiped where the entire domain is discretized by a uniform fixed 3-D finite-difference mesh and has a standard staggered MAC cell arrangement ([Harlow & Welch, 1965](#)). The velocity components  $\bar{u}$ ,  $\bar{v}$  and  $\bar{w}$  are defined on the corresponding cell faces while the scalar variables (pressure  $\bar{p}$  and the distance function  $\psi$ ) are located at the cell centres. All spatial derivatives are approximated by second-order centred differences. The velocity field is solved by a parallel generalized minimal residual (GMRES) method ([Saad, 2003](#)) and the pressure field by a modified parallel 3-D multigrid solver ([Kwak & Lee, 2004](#); [Shin et al., 2017](#)). Parallelisation is achieved using an algebraic domain decomposition where communication across processes are handled by message passing interface (MPI) protocols. Further details of the numerical framework used in this work can be found in [Shin \(2007\)](#); [Shin et al. \(2017, 2018\)](#); [Shin and Juric \(2009\)](#).

The chosen pitched-blade turbine shown in [figure 1](#) and described in the beginning of this section is built using a combination of primitive geometric objects (planes, cylinders, and rectangular blocks) where each object is defined by a static distance function  $\psi(x, y, z)$ , positive in the fluid and negative in the solid. The resulting shape in [figure 1\(c\)](#) corresponds to the iso-value  $\psi(x, y, z) = 0$ . Details on how to construct similar complex objects are described in [Kahouadji et al. \(2018\)](#).

For (2.2), (2.8) and (2.10), we use the single-field formulation for the density  $\rho$  and viscosity  $\mu$ :

$$\left. \begin{aligned} \rho(\mathbf{x}, t) &= \rho_g + (\rho_l - \rho_g) \mathcal{H}(\mathbf{x}, t), \\ \mu(\mathbf{x}, t) &= \mu_g + (\mu_l - \mu_g) \mathcal{H}(\mathbf{x}, t), \end{aligned} \right\} \quad (2.11)$$

where the subscripts  $g$  and  $l$  designate the gas and liquid phases, respectively. The indicator function,  $\mathcal{H}$ , is a Heaviside function, zero in the gas phase and unity in the liquid phase; numerically,  $\mathcal{H}$  is resolved with a smooth transition across three to four grid cells and is generated using a vector distance function  $\varphi(\mathbf{x})$ , positive for the liquid phase and negative for the gas phase, and is computed directly from the tracked interface ([Shin & Juric, 2009](#)). The gas phase is considered as air, with constant physical properties at 20 °C ( $\rho_g = 1.205 \text{ kg m}^{-3}$  and  $\mu_g = 1.825 \times 10^{-5} \text{ Pa s}$ ). The liquid phase corresponds to either water or glycerine with the following properties:  $\rho_l = 1000 \text{ kg m}^{-3}$ ,  $\mu_l = 10^{-3} \text{ Pa s}$  and  $\sigma = 0.0725 \text{ N m}^{-1}$  or  $\rho_l = 1261.08 \text{ kg m}^{-3}$ ,  $\mu_l = 1.4 \text{ Pa s}$  and  $\sigma = 0.064 \text{ N m}^{-1}$ , for water and glycerine, respectively. Simulations with glycerine and water allow us to compare the two-phase mixing phenomena associated with laminar and turbulent flow regimes, respectively. The laminar simulations were carried out using a full direct numerical simulation (DNS) approach, whereas the LES Smagorinsky–Lilly model described above was deployed for the turbulent cases.

### 3. Validations

In the previous section, we have detailed the governing equations and the numerical scheme that accounts for the fluid–structure interaction applied to a turbulent multiphase mixing vessel. Before moving to the results section, it is crucial to validate this new numerical framework that combines both a direct forcing method for the impeller motion and the hybrid front-tracking/level-set method for tracking the interface in the context of a turbulent two-phase flow in an agitated vessel. [Figure 2\(a\)](#) provides evidence of mesh-independence of our numerical solutions by showing the normalised minimum position of the interface which is often located at the axis  $r = 0$  generated via the LES and DNS approaches. Global meshes of  $192 \times 192 \times 256$  and  $256 \times 256 \times 384$  are used and results are presented for water agitated at a constant frequency  $f = 1/T = 8 \text{ Hz}$  ( $Re \sim 2.0 \times 10^4$ ,  $Fr \sim 0.33$  and  $We \sim 110$ ). It is clear from [figure 2\(a\)](#) that both resolutions lead to accurate predictions of the interface deflection for both the DNS and LES approaches. It is also well known through the previous works of [Piva and Meiburg \(2005\)](#) and [Kahouadji \(2011\)](#) that the physical quantity that plays a major role in interface deflection is the azimuthal velocity distribution along the interface,  $u_\theta \sim r$ , close to the shaft. Therefore, even for turbulent regimes, the interface can be accurately captured via the DNS or LES approaches. Thus, the resolution used in the rest of this paper is globally  $256 \times 256 \times 384$  with a constant LES model unless specified otherwise. As



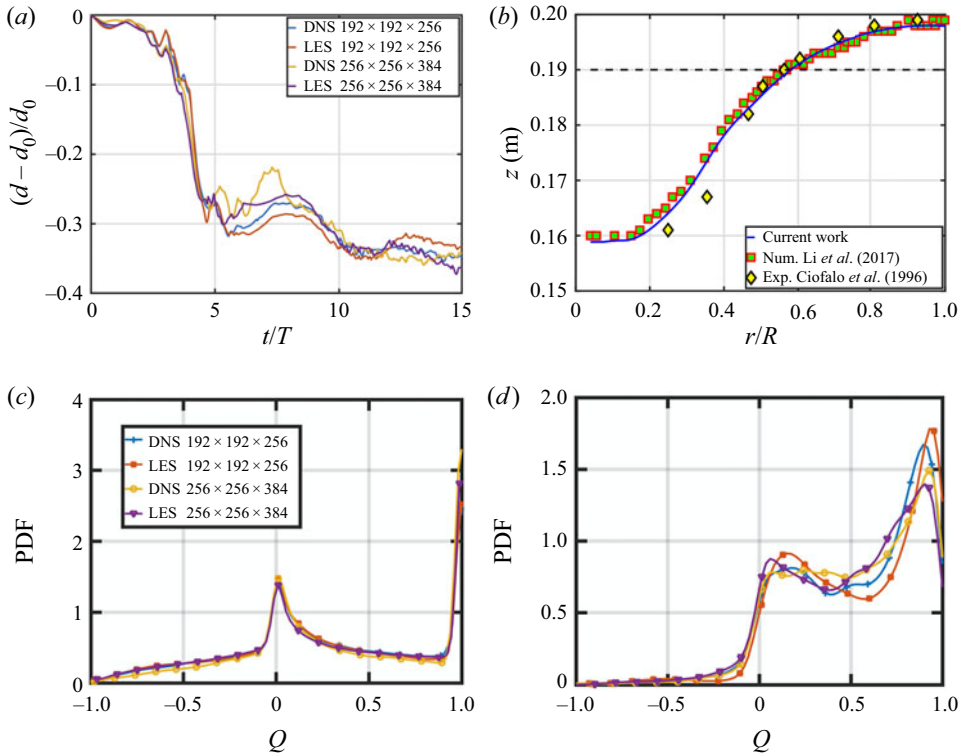


**Figure 2.** Validation of our numerical framework and mesh dependence predictions generated via LES and DNS approaches with the following parameters:  $f = 1/T = 8 \text{ Hz}$ ,  $Re \sim 2.0 \times 10^4$ ,  $Fr \sim 0.33$  and  $We \sim 110$ , using water properties: (a) minimal vertical position of the interface normalised by the position at the axis  $r = 0$ ; (b) comparison with a benchmark case for a developed interface shape from Ciofalo et al. (1996) and Li et al. (2017); (c) probability density function estimated via the kernel density estimation (KDE) of the flow topology parameter  $Q$ , as defined by Soligo, Roccon, and Soldati (2020), for the liquid phase; (d) same as panel (c) but only at the gas–liquid interface.

mentioned in the previous section, for the laminar cases discussed in § 4.1, we set the parameter  $C_s = 0$  in (2) and use a full DNS approach.

We also provide further validation involving a direct comparison with previous works of Ciofalo et al. (1996) and Li et al. (2017). The configuration here consists of a cylindrical tank with diameter of 0.19 m and height of 0.30 m filled with a liquid of initial height of 0.19 m and agitated by a pitched blade turbine at  $194 \text{ r min}^{-1}$  ( $f \sim 3.23 \text{ Hz}$ ) located at a distance  $\sim 6.3 \text{ cm}$  from the bottom. More details of this configuration can be found in Ciofalo et al. (1996) and Li et al. (2017). The physical properties of the liquid working medium are those of water ( $\rho_l = 998 \text{ kg m}^{-3}$ ,  $\mu_l = 0.00103 \text{ Pa s}$ ) and the surface tension coefficient between the phases (air and water) is set as  $0.0732 \text{ N m}^{-1}$ . As depicted in figure 2(b), our numerical framework is capable of reproducing accurately different stirring configurations. Note that our computation is purely three-dimensional and the resulting interface is axisymmetric.

After a convincing mesh-grid dependence shown in figure 2(a) and a like-to-like comparison with both Ciofalo et al. (1996) and Li et al. (2017), we extend further this validation section by providing statistics on flow characteristics by introducing a flow ‘topology’ parameter,  $Q$ , which can identify regions in the domain where the flow is either solely rotational ( $Q = -1$ ), shear ( $Q = 0$ ) and/or purely elongational ( $Q = 1$ ). This flow topology parameter  $Q$  is calculated as the second invariant of the

velocity gradient tensor  $\nabla \mathbf{u}$  as follows:

$$Q = \frac{D^2 - \Omega^2}{D^2 + \Omega^2}, \quad (3.1)$$

where  $D^2 = D : D$  and  $\Omega^2 = \Omega : \Omega$ , where  $D$  and  $\Omega$  denote the rates of deformation and rotation tensors (Soligo et al., 2020), respectively. Figures 2(c) and 2(d) provide information on the purely rotational, shear or elongational flow types occurring for  $f = 8$  Hz in the entire domain (see figure 2c) and also only on the deformed interface (see figure 2d). Further details on how  $Q$  is distributed in the flow are provided in § 4.2.1, but to strengthen this validation part, both resolutions for the DNS or LES approaches provide similar probability density functions (PDFs) for  $Q$ .

In conclusion, the examples shown in figure 2 inspire confidence in our new numerical framework which combines an LES model and a direct forcing method for an FSI (fluid–structure interaction) configuration, within the context of a hybrid front-tracking/level-set method for the advection of the interface. Another novelty, and a significant challenge which this study will address, is to simulate the aeration regime that features a multitude of interfacial singularities such as breakup and coalescence at large density ratios,  $\sim 10^3$ ; this is notoriously troublesome for numerical procedures previously used for the simulation of two-phase flows.

## 4. Results and discussion

We begin the presentation of our results by describing the flow associated with the case of glycerine (§ 4.1) wherein the interface is slightly deformed. In § 4.2, we replace glycerine with water and highlight the emergence of complex vortical structures and a highly deformed surface; a large range of rotating frequencies, from  $f = 5$  to 9.5 Hz, is covered. The mechanisms leading to aeration are studied in § 4.3 by close examination of the transition boundary between the separated and dispersed flows. Finally, § 4.4 focuses on the situation wherein air is entrained into the water across a highly deformed interface leading to bubbly mixing.

### 4.1. Laminar mixing (viscous regime)

The typical flow in the laminar regime is summarised in figure 3. Here, glycerine is chosen as the liquid phase and the rotation frequency is restricted to  $f = 1/T = 8$  Hz so that the flow regime remains laminar and the free surface deformation small, characterised by the following values of the relevant dimensionless numbers:  $Re \sim 18$ ,  $Fr \sim 0.33$  and  $We \sim 157$ . The free surface deformation is defined as ‘small’ provided the amplitude of the deflection to the horizontal, divided by the characteristic length scale  $D_i$ , does not exceed 10%.

A centrifugal force is generated in the vicinity of the rotating blades causing the glycerine solution to spiral out toward the tank periphery (see figure 3a). This spiralling motion reaches the fixed vessel wall inducing the formation of two Stewartson boundary layers (Kahouadji & Martin Witkowski, 2014; Poncet, 2005; Stewartson, 1953) at the top and bottom peripheries. The fluid motion separates and reaches both the free surface and the bottom of the tank, it then decelerates by a centripetal spiral motion toward the rotating shaft (rotation axis) above (below) the impeller; this is analogous to the behaviour reported previously in the literature for rotating disks (Daube, 1991; Kahouadji & Martin Witkowski, 2014; Piva & Meiburg, 2005; Spohn, 1991; Spohn et al., 1993, 1998). The flow is not axisymmetric, and one can see in figures 3(a) and 3(b) that the position of the rotating blades matter in terms of understanding the reasons underlying the flow patterns. Under the pumping effect generated by the rotating blades, the fluid returns toward the rotating hub and blades by an upward swirling motion around the  $z$ -axis from the bottom and by a downward swirling motion around the rotating shaft (see figure 3a,b).

The temporal evolution starting from a static initial condition  $t = 0 \times T$  up to  $t = 1.375 \times T$  is shown in figure 3(c), which depicts the streamlines in the horizontal plane immediately below the hub as well



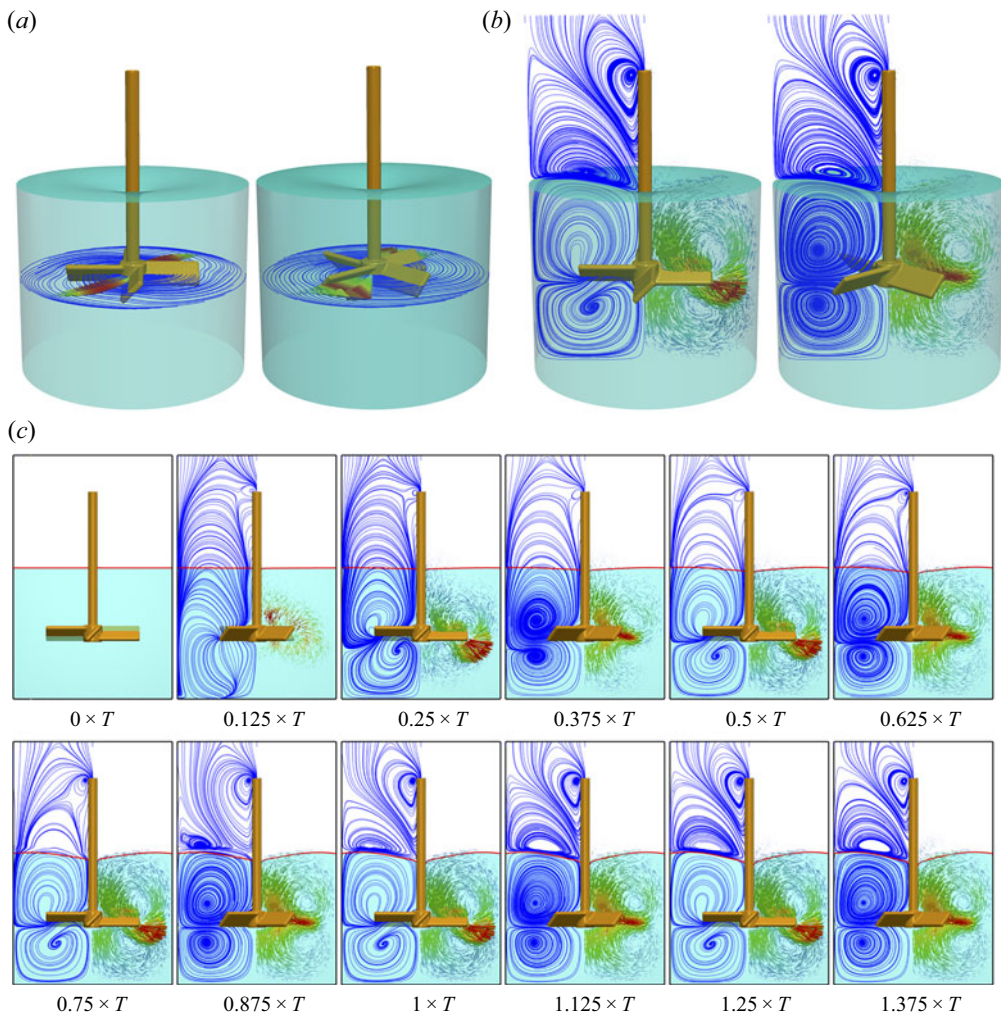


**Figure 3.** Laminar mixing flow for the case of glycerine with  $f = 1/T = 8$  Hz for which the dimensionless numbers are  $Re \sim 18$ ,  $Fr \sim 0.33$  and  $We \sim 157$ . Flow visualisation of the streamlines in the horizontal plane located at  $z = 3.95$  cm (a), and vertical plane  $y = 0$  (b); (c) snapshots of the streamlines in the  $y = 0$  plane that illustrate the temporal evolution of the flow starting from rest (see supplementary movie ‘Animation-Fig3.avi’ available at <https://doi.org/10.1017/flo.2022.24>).

as in the  $y = 0$  plane. From this figure, we can see that the free surface shape becomes essentially steady for  $t > T$ . This has similarity with the work of Kahouadji and Martin Witkowski (2014) who studied the free surface rotating flow generated by a rotating disk located at the bottom of a fixed cylindrical tank by solving the steady and axisymmetric Navier–Stokes equations using a vorticity-streamfunction formulation. Assuming a developed steady state, Kahouadji and Martin Witkowski (2014) considered the interface as a streamline. In the present case, as shown in figure 3(c), the streamlines cross the interface for  $t < T$  indicating interfacial motion, whereas for  $t > T$ , the interface becomes a streamline and remains steady. It is also noteworthy that although the interfacial shape is steady and axisymmetric for  $t > T$ , the liquid flow is periodic in its azimuthal direction with a periodicity mode of 4, reflecting the impeller geometry which comprises four blades. Finally, we draw attention to the time required to make the flow quasi-steady:  $t \sim T = 1/f = 1/8$  (s); this is in contrast to the cases which will be discussed below where, typically, 10 or  $20 \times T$  are required to reach a quasi-steady state.

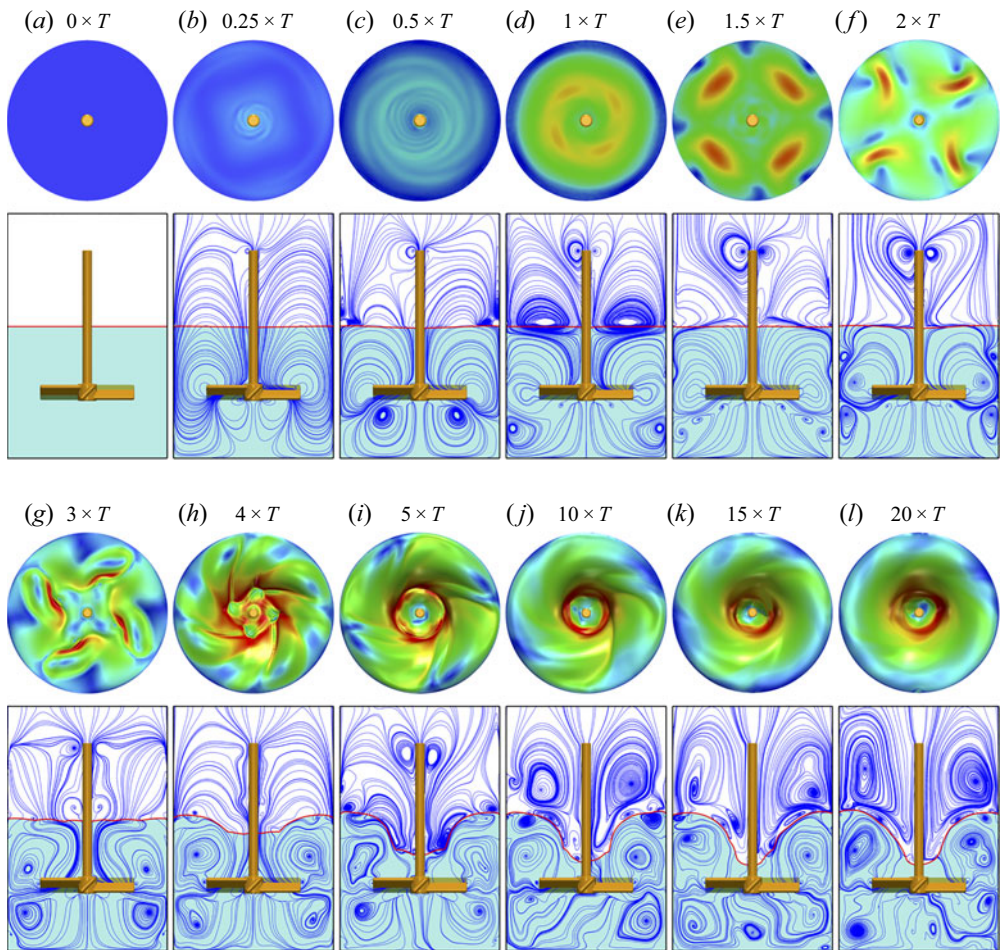


**Figure 4.** Spatio-temporal evolution of the flow for water: vortical structures and interface shapes coloured by velocity magnitude shown in the lower and upper figures in every panel, respectively, for  $f = 1/T = 8$  Hz. The dimensionless numbers are  $Re \sim 2.0 \times 10^4$ ,  $Fr \sim 0.33$ ,  $We \sim 110$  (see supplementary movie ‘Animation-Fig4.avi’).

#### 4.2. Turbulent vortex mixing

We replace the highly viscous glycerine with water and keep the frequency at  $f = 8$  Hz so that the flow is characterised by  $Re = 2.0 \times 10^4$ ,  $Fr = 0.33$  and  $We = 110$ , which indicates that it is expected to be turbulent and accompanied by large interfacial deformations. We show in figure 4 the spatio-temporal behaviour of the flow for  $f = 1/T = 8$  Hz starting from a static initial state until a steady state is reached for  $t = 20 \times T$ . It is seen that the free surface shape remains quasi-flat until the impeller has rotated 1.5 cycles (see figure 4a–e). However, in spite of this, for the velocity magnitude on the interface, figure 4(d–j) shows that the velocity disturbance experiences a periodic distribution along its azimuthal direction with a wave number equal to 4, a symmetry that once again reflects the impeller 4-blade geometry. At  $t = 2 \times T$ , the interface starts to deform (see figure 4f–l) where the velocity gradient is high, leading to a periodic azimuthal interface deflection with a wave number of 4 being preserved. The interface continues to undergo spatio-temporal variations until reaching a quasi-steady and approximately axisymmetric state beyond  $t = 10 \times T$ , as shown in figure 4(j–l), which is characterised by maximal interfacial deflection.



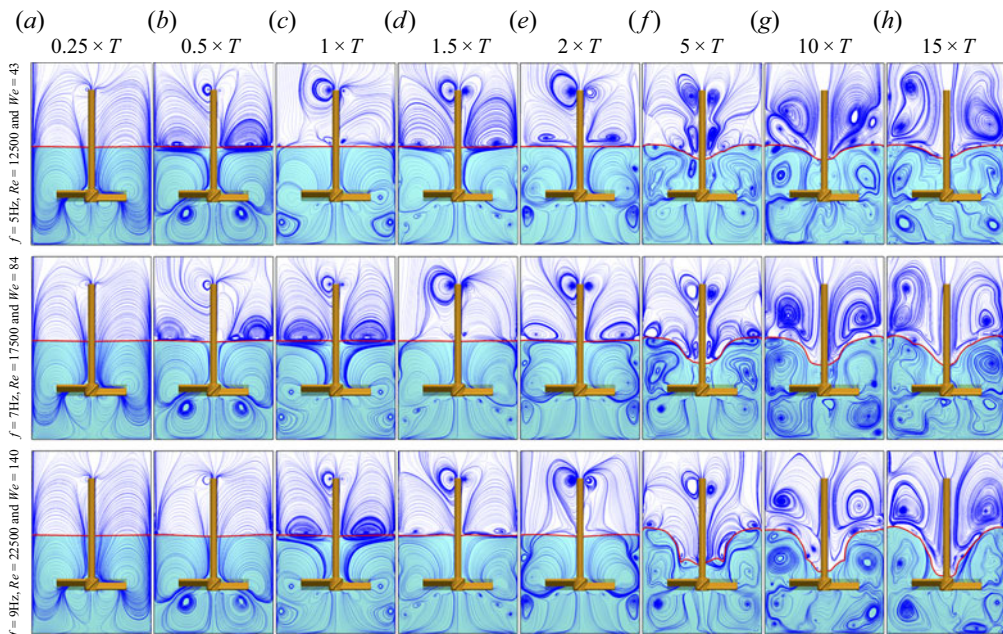


**Figure 5.** Spatio-temporal evolution of vortical structures in water for  $f = 1/T = 5, 7$  and  $9$  Hz, from top to bottom, respectively, and  $t = 0.25 \times T - 15 \times T$ . The corresponding Reynolds and Weber number combinations are  $(Re, We) = (12\,500, 43)$ ,  $(17\,500, 84)$  and  $(22\,500, 140)$ , respectively (see supplementary movie ‘Animation-Fig5.avi’).

The evolution of the vortical structures in the vertical plane shows the existence of very rich dynamics, as depicted in figure 4. At early times ( $t \sim 0.25 \times T$ ), the impeller blades generate a large primary vortex that starts at the blade tips towards the bottom of the vessel and then moves upward near the vessel wall towards the interface. A secondary vortex is also generated under the impeller blades, which rotates radially in the opposite direction compared to the primary vortex. This secondary vortex is generated from the bottom of the impeller hub and grows until being replaced by a two dipole-vortex, one above and the other below the impeller blades (see the streamlines in figure 4(c,d) for  $t = 0.5$  and  $1 \times T$ ).

At  $t = 1.5 \times T$ , the bottom vortex dissipates and we notice the creation of Kelvin–Helmholtz vortices that merge at  $t = 2 \times T$  into a single vortex below the impeller blades (see the streamlines in figure 4e,f). These Kelvin–Helmholtz vortices are generated due to the fact that the primary top vortex rotates faster (due to the presence of the interface) than the secondary bottom vortex (due to the no-slip condition at the bottom of the vessel) and creates a large shear zone between these two vortices. For  $t \geq 2 \times T$ , the Kelvin–Helmholtz vortices give way to two large counter-rotating vortices and a small vortex breakdown underneath the impeller hub, a well-known phenomenon in the context of a rotating disk inside a closed cylindrical tank (i.e. a rotor-stator configuration Daube, 1991; Kahouadji, 2011; Spohn, 1991; Spohn et al., 1998). These vortical structures described for  $f = 8$  Hz are also observed for the entire range of frequencies  $f \leq 9$  Hz, as shown in figure 5, which depicts the spatio-temporal evolution of the interface and vortical structures in a two-dimensional plane for  $f = 5, 7$  and  $9$  Hz for  $t = 0.25 \times T - 15 \times T$  (see also the supplementary movie ‘Animation-Fig5.avi’). Further inspection of figure 5 reveals strong qualitative similarities amongst the vortical structures for this range of frequencies (and  $Re$  and  $We$ ) for  $t \leq 2 \times T$ .

Figure 6(a–f) depicts snapshots of the interface shape, and accompanying structures in the vorticity and pressure fields at  $t/T = 20$  for  $f = 5 - 9.5$  Hz. It is clear that the salient points highlighted for  $f = 8$  Hz in figure 4 are observed for the entire frequency range. Figure 6(g) shows the temporal evolution of the

global kinetic energy of the flow,

$$\kappa = \left( \int \int \int \rho u^2 \, dx \, dy \, dz \right), \quad (4.1)$$

normalized by its value at saturation  $\kappa_\infty = \kappa_{(t \rightarrow \infty)}$  and [figure 6\(h\)](#) shows the variation of the minimum position of the interface with time for the range of frequency  $f = 5$  to 9.5 Hz. For  $f = 5$  Hz, the interface deflection is small compared to other cases and a vortex breakdown attached to the interface occurs; this phenomenon is also observed for rotating disks inside an open cavity ([Kahouadji & Martin Witkowski, 2014](#); [Piva & Meiburg, 2005](#); [Spohn, 1991](#); [Spohn et al., 1993, 1998](#)). In certain cases, there is an appearance of a small vortex at the bottom corner of the vessel or at the top corner (see [figure 6c](#) for  $f = 7$  Hz). For  $f = 9.5$  Hz, the interface just reaches the hub of the impeller (see [figure 6f](#)). For this set of parameters, this frequency represents the limit for rapid mixing without the entrainment of bubbles into the water phase.

At  $t = 20 \times T$ , we consider the flow to be quasi-steady as the curves corresponding to [figure 6\(g,h\)](#) flatten, particularly for the range  $f = 5$ –8 Hz. For  $f = 9$  and 9.5 Hz, although the kinetic energy appears to plateau for  $t \geq 10 \times T$ , the minimal interfacial position exhibits small-amplitude, high-frequency oscillations due to the interfacial interactions with the impeller hub.

The pressure field shown in [figure 6](#) for all values of  $f$  illustrates the dominance of the vortical structures on the pressure field. For small rotation frequency values ( $f \leq 5$  Hz), the behaviour of the pressure is hydrostatic, decreasing linearly as a function of  $z$ -direction. This type of pressure field distribution is observed for  $f = 5$  Hz (see [figure 6a](#)). Increasing the frequency up to 6 Hz, the pressure field still varies linearly through the  $z$ -direction; however, a depression zone is noticed at the back of the blades (see pressure field in [figure 6b–f](#)). This depression is a characteristic of flows past an obstacle, which means that in the rotating blades reference, the front and back of the blades are zones of high and low pressure, respectively. In addition to these low and high pressure zones near the blades, we can notice that for high values of rotation frequency ( $f \geq 7$  Hz), the eddy structures break the hydrostatic form of the pressure field and a high pressure zone is localised only near the bottom outer edge of the vessel.

#### 4.2.1. Flow topology in turbulent mixing

To provide further insights into the rich turbulent dynamics taking place in the cases discussed above, the relationship between the types of flow and the distinguishable vortical structures emerging is considered herein. To do this, we have chosen to calculate the flow topology parameter  $Q$ , described by [Soligo et al. \(2020\)](#) and defined in (3.1), and superpose it with the vortical structures addressed earlier, as shown in [figure 7](#). The parameter  $Q$  that allows us to identify among three types of flows, solely rotational, shear and elongational flow corresponding to  $Q = -1, 0, 1$ , respectively, shows that the hub of most vortical structures are purely rotational especially the region below the impeller hub where vortex breakdown appears. Furthermore, the air phase is mostly dominated by elongational flow. It is also interesting to note that despite the fact that the impeller shaft rotates, its radial vicinity is also dominated by an elongational flow due to the centrifugal Eckman pumping effect that drags not only the interface downward but also the air in that radial vicinity of the rotating shaft. Moreover, it is also noticeable that the air just above the interface is predominantly in shear flow due to its centripetal motion.

On the interface, close inspection of the flow topology parameter  $Q$  reveals certain similarities for all values of  $f$  varying from 5 to 9.5 Hz. First, near  $r = 0$ , the interface ( $r \sim 0$ ) is always purely rotational as it corresponds to the part of the interface that is immersed inside the rotating shaft. The parabolic part of the interface is a mixture of both shear and elongation, but close to the wall is more dominated by a shear type of flow. Finally, even if it is difficult to describe with precision this chaotic behaviour of  $Q$ , the probability density function of  $Q$ , provided in the validation section, indicates the amounts of rotation, shear and elongational flow types that occur in such turbulent flow (see [figure 2c,d](#)).

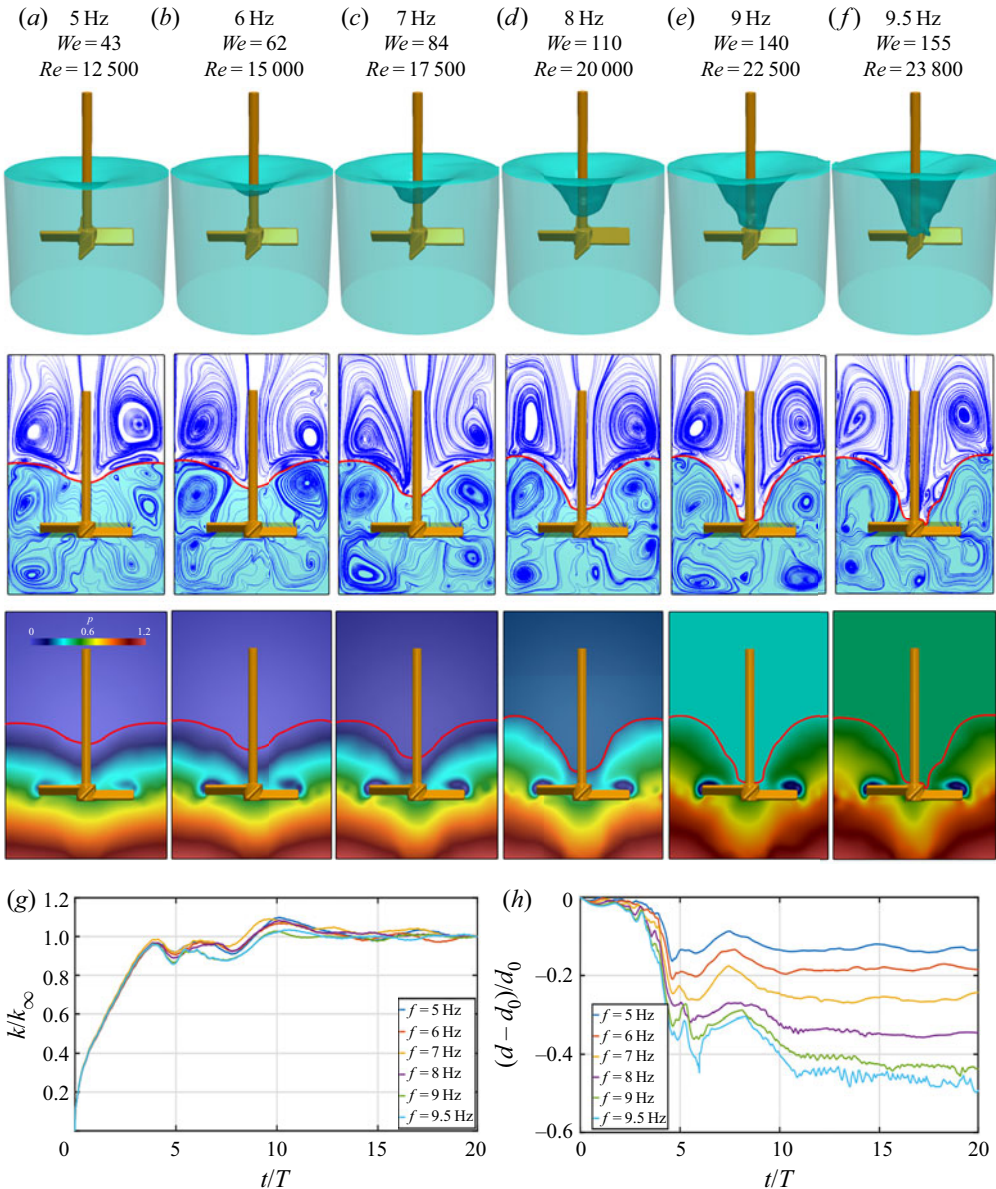


**Figure 6.** Interface shape, vortical structures and pressure fields in a two-dimensional vertical plane at  $t/T = 20$  for  $f = 5, 6, 7, 8, 9$  and  $9.5$  Hz, (a–f), respectively; (g,h) temporal evolution of the kinetic energy normalized by its value at saturation  $\kappa_\infty = \kappa(t \rightarrow \infty)$  and minimum interface position normalized by its initial value (see supplementary movie ‘Animation-Fig6.avi’).

### 4.3. Transition to aeration

In this section, we will focus on the air–water system and elucidate mechanisms that lead to entrainment of air bubbles into the water phase through careful examination of the transition boundary between the vortex and bubbly mixing regimes. To perform accurate simulations of the onset of aeration, all simulations presented in this section are performed using  $4 \times 4 \times 6 = 96$  subdomains, with a Cartesian structured grid of  $64^3$  per subdomain, which gives a global structured mesh of  $256 \times 256 \times 384$ .



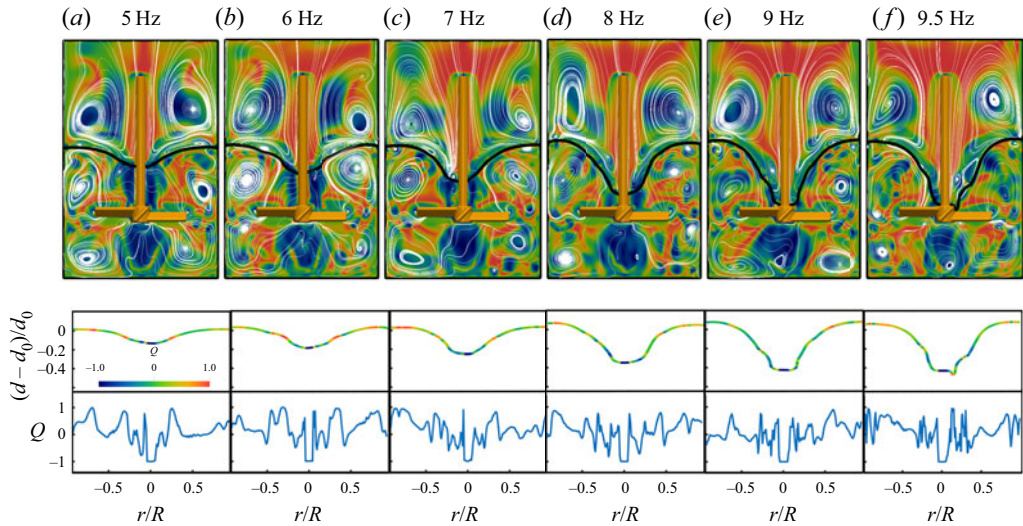


**Figure 7.** Top row: flow topology  $Q$  accompanied by vortical structures in the vertical plane  $y = 0$  for frequency  $f = 5, 6, 7, 8, 9$  and  $9.5$  Hz, shown in panels (a–f), respectively, and  $t/T = 20$ . Bottom row: vertical position of the gas–liquid interface normalised by its initial position  $d_0$  and coloured by the flow topology  $Q$  with the corresponding radial variation of the interfacial  $Q$  plotted underneath for the same  $f$  and  $t/T$  values as those used to generate the top row results.

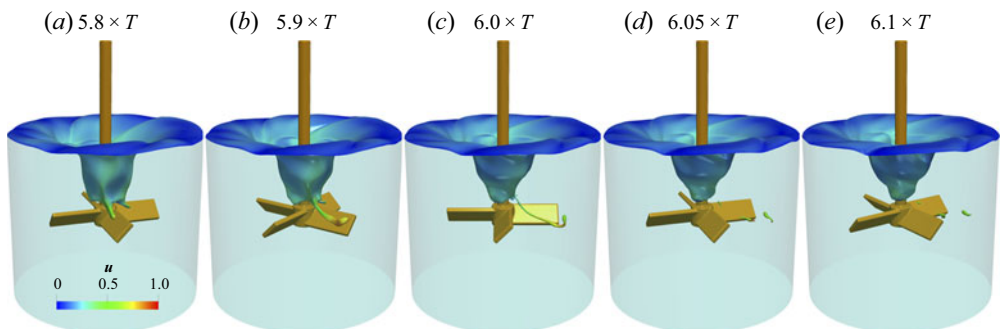


**Figure 8.** Spatio-temporal evolution of the mixing behaviour for  $f = 1/T = 10$  Hz,  $Re = 25\,000$  and  $We = 172$  highlighting the onset of aeration.

Figure 8 depicts the interfacial dynamics associated with the  $f = 10$  Hz case, characterised by  $Re = 25\,000$  and  $We = 172$ . The results presented thus far were generated by starting from an initially flat interface and a velocity field at rest ( $\mathbf{u} = \mathbf{0}$ ). Using this initialisation, it is seen clearly that the interface, which interacts with the impeller hub, undergoes breakup leading to the formation of three small bubbles that are entrained into the water phase. If, however, the simulation is initialised starting from the steady-state associated with the  $f = 8$  Hz case, but with  $f = 10$  Hz, then we find that the outcome (not shown) corresponds to a vortex mixing regime, similar to that shown in figure 6(f).

To elucidate the mechanisms underlying aeration, we focus on the case wherein the flow is started impulsively from an initially stationary flat-interface state. As a result of the impeller rotation, a low pressure region forms near the impeller hub that leads to a large interfacial deflection and the formation of a thin air ligament at the back of one of the blades; this is a consequence of the centrifugal forces that drive ligament elongation in the radial direction away from the hub. The ligament eventually undergoes a Rayleigh–Plateau instability and breaks up into three small bubbles (see figure 8c–e). Thus, the route



to bubble creation, and subsequent aeration of the water phase, involves three successive mechanisms: (i) a sufficiently strong centrifugal force able to deform the interface rapidly towards the impeller hub; (ii) ligament formation that grows radially behind a blade; (iii) a Rayleigh–Plateau-driven breakup of the ligament. The example shown in [figure 8](#) features the formation of only one air ligament and its breakup. We will show that further increase in rotating frequency causes simultaneous entrapment and growth of multiple ligaments, leading to a more violent transition to the bubbly mixing regime.

#### 4.4. Bubbly mixing

After the brief discussion of the mechanisms underlying aeration mixing, we now increase the impeller rotation frequency to  $f = 11$  Hz ( $Re = 27\,500$  and  $We = 209$ ) for which the outcome is very bubbly with a total number of air bubbles being of the order of hundreds dispersed inside the water phase. We have performed this calculation using both the DNS and LES approaches and simulations with the former exhibit interesting phenomena such as the bursting effect with the main interface. [Figure 9](#) shows the spatio-temporal evolution of the flow, using DNS, where it is seen that the initially flat interface undergoes a rapid deflection (see [figure 9a–c](#)) towards the impeller blades (see [figure 9e–f](#)) with some interfacial pinchoff without significant ligament formation and breakup (see [figure 9g–h](#)).

At  $t = 4.25 \times T$ , four air ligaments are formed, which grow quickly in the radial direction and break up into many bubbles (see [figure 9i,j](#)). The resulting air-ligaments forming behind each blade are not as thin as in the case described for  $f = 10$  Hz (see [figure 8](#)). As highlighted through [figure 9\(j,k\)](#), thick shaped air ligaments will breakup and disperse all around the liquid water phase. This process continues and produces a myriad of multiscale air-bubbles. Some of these bubbles have the shape of elongated thin air ligaments, also dispersed in the water phase, and eventually breakup later into smaller bubbles.

The flow is also accompanied by a series of coalescence events that occur between bubbles inside the water phase as well as with the main top interface. Small bubbles usually remain in the water phase but larger bubbles, due to buoyancy, rise to the top. When any bubble reaches the main top interface, it bursts and sometimes ejects some liquid-droplets above the interface (see [figure 9n,o](#)).

In [figure 10](#), we have isolated several ‘singular’ events that involve topological transitions occurring in this type of bubbly mixing. [Figure 10\(a\)](#) highlights a coalescence event between a small bubble and the main interface. These snapshots in [figure 10\(a\)](#) are given at the following times, from top to bottom,  $t/T = 5.92$ ,  $5.94$  and  $5.96$ , respectively. We can notice that the small bubble coalesces with the vertical part of the main interface that surrounds the impeller shaft. In [figure 10\(b\)](#), we have also isolated the breakup event of a ligament. We can notice a rapid coalescence of a tiny bubble with this ligament before experiencing two interfacial breakups later.

[Figure 10\(c\)](#) shows the temporal evolution of a bubble bursting through the main top interface, generating liquid ligaments above this interface and finally breaking up into a multitude of droplets that will fall back to the liquid bulk later on. In contrast to the coalescence described in [figure 10\(a\)](#), when a bubble hits the top interface, it bursts. However, if a bubble hits the vertical part of the main interface, the outcome corresponds to a simple coalescence process. Furthermore, for the latest snapshot of [figure 10\(c\)](#), we count a total of 503 bubbles dispersed inside the bulk of the water phase and also a total 33 water drops. Some of the water drops are located above the main top interface (see the latest snapshots in [figure 10c](#)), but some others are encapsulated within some large bubbles inside the bulk water phase.

At this stage of the mixing process, it is interesting to follow the temporal evolution of the bubble sizes during the aeration process. We can notice through [figure 9](#) that the appearance of bubbles in the liquid bulk starts at time  $t/T \approx 4.5$  (see [figure 9g](#)). Moreover, the flow can be considered as ‘bubbly’ only at  $t/T \approx 5.5$  ([figure 9k](#)). It is possible to isolate all  $n$  bubbles dispersed within the water phase, calculate the volume of each individual bubble  $\mathcal{V}_{b,i}$  ( $i = 1, n$ ) and deduce an approximation of its diameter  $d_{b,i} = (6\mathcal{V}_{b,i}/\pi)^{1/3}$ . [Figure 11\(a\)](#) represents the probability density function of bubble size distribution for  $t/T = 10$  using both LES and DNS formulations. Most of the bubble sizes are smaller than the average value  $d_{bm}$ . The probability density functions are quasi-similar (see [figure 11a](#)).

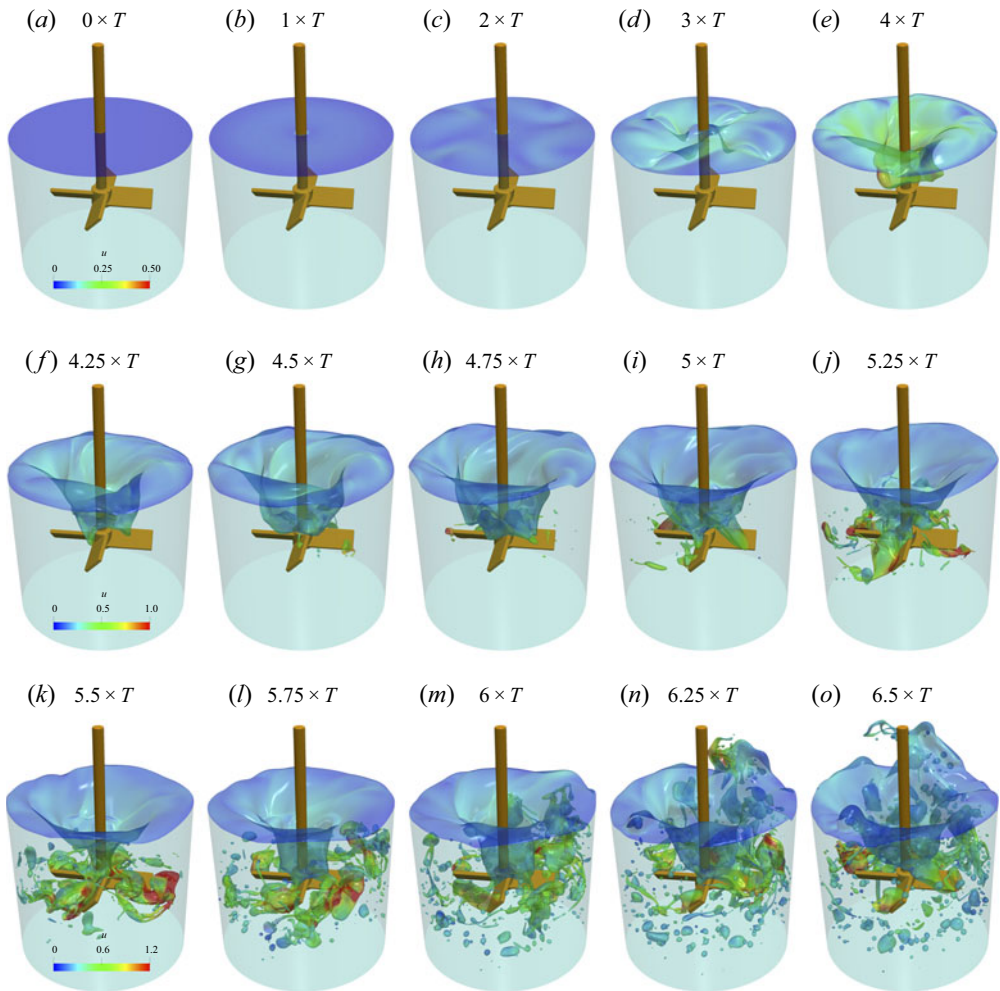


**Figure 9.** Spatio-temporal evolution for bubbly mixing with  $f = 1/T = 11$  Hz,  $Re = 27\,500$  and  $We = 209$ .

Finally, from an engineering perspective, it is crucial to estimate the air bubble volume dispersed inside the water phase. As mentioned in the introduction, for some applications, bubbles are desirable and for others, their presence must be avoided. However, if these air bubbles are produced during a mixing process, it is important to estimate the temporal evolution of the gas holdup,  $\varepsilon$ :

$$\varepsilon(t) = \mathcal{V}_b / (\mathcal{V}_b + \mathcal{V}_l), \tag{4.2}$$

which is the ratio of the volume of the air phase entrained within the water,  $\mathcal{V}_b = \sum_{i=1}^n \mathcal{V}_{b,i}$ , to the total volume of air and water within the stirred vessel;  $\mathcal{V}_l = \pi D_b^2 h / 4$  is the volume of the water phase. In [figure 11\(b\)](#), we show the evolution of the gas holdup  $\varepsilon(t)$  highlighting its maximum value at  $t/T \approx 6.25\text{--}6.5$  beyond which the dynamic equilibrium amongst bubble formation, coalescence and breakup leads to a steady  $\varepsilon$ . Inspection of [figure 11\(b\)](#) reveals that the bubbly steady-state using both DNS and LES is reached for  $t/T \geq 8$  with approximately 1.9% of air dispersed in the water bulk. The difference between these approaches is in the interval  $t/T \approx 5.5\text{--}8.0$ , where DNS predicts more bubbles compared to LES.

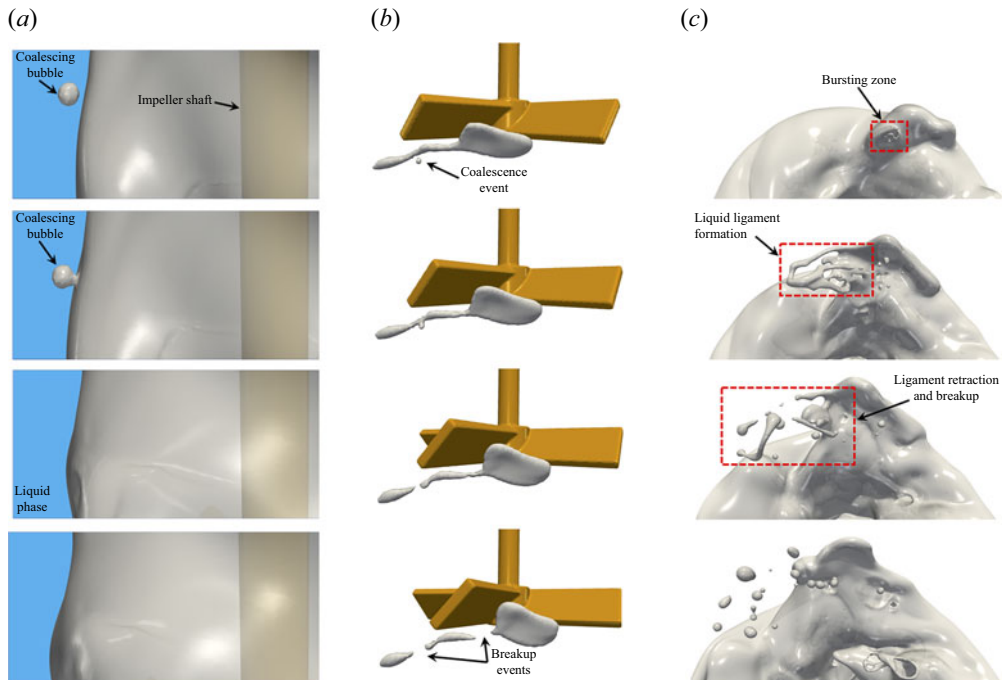


**Figure 10.** Flow snapshots for  $f = 1/T = 11$  Hz,  $Re = 27\,500$  and  $We = 209$  showing bubble–interface coalescence, ligament breakup and bubble bursting through the interface in panels (a–c), respectively.

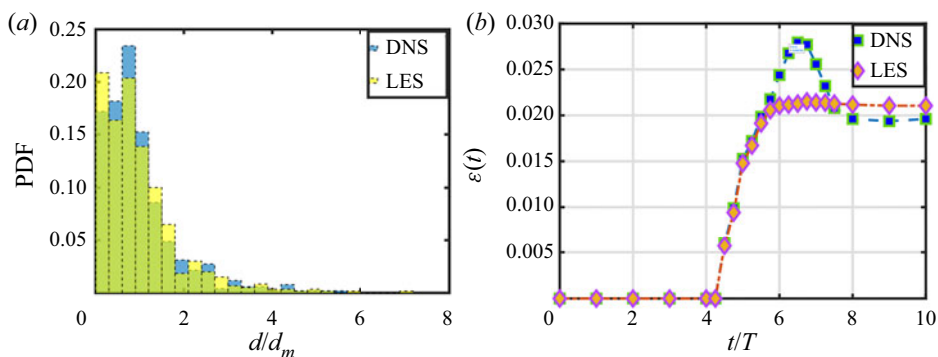


**Figure 11.** (a) Probability density function histogram of bubble size inside the liquid bulk, normalised by the average bubble diameter,  $d_{bm}$ , associated with the time  $t/T = 10$ ; (b) temporal evolution of the gas holdup  $\varepsilon(t)$  generated using the DNS and LES approaches. The rest of the parameter values are the same as those used to generate figure 7.

## 5. Conclusion and perspectives

In this paper, we have studied numerically the complex dynamics occurring during air–liquid mixing using a pitched blade turbine. The motion of the impeller and the fluid–structure interaction is computed by a direct forcing method within a general solver for multiphase flows (Shin et al., 2017). We have shown that vortical structures are similar for any frequency below the aeration limit. These vortical structures correspond to Kelvin–Helmholtz, blade tip, end wall and wall breakdown vortices. Aeration occurs for a sufficiently large rotational frequency, and we highlight the importance of the initial state (from rest or from an already developed flow). Future research avenues for study are to investigate further the

physics of the aeration (for frequencies larger than 10 Hz) and to generalise this study through variation of the initial liquid height, the clearance and the diameter ratio between the impeller and the cylindrical tank. Another type of multiphase mixing process that has not been studied here and occurs for high frequencies,  $f \geq 15$  Hz, is ‘air envelopment’ mixing. At very high rotation frequencies, the air phase will envelop the entire impeller during the rotation. Similarly, a major route of research in turbulent mixing systems focuses on emulsification processes (liquid–liquid flows), specifically on expanding the understanding of the hydrodynamic phenomena which are similar to those studied here but in the context of liquid–liquid systems, including droplet breakage under turbulent conditions beyond the well-known Kolmogorov–Hinze theory (Håkansson, 2019). Finally, industrially relevant flow systems involving fluids with complex rheological behaviour, and variable surface tension due to the presence of surfactants, could also be modelled in the future too, since the recent paper of Shin et al. (2018) has paved the way towards a numerical method which can handle such scenarios.

**Supplementary movies.** Supplementary movies are available at <https://doi.org/10.1017/flo.2022.24>.

**Acknowledgements.** D.J. and J.C. acknowledge support through HPC/AI computing time at the Institut du Développement et des Ressources en Informatique Scientifique (IDRIS) of the Centre National de la Recherche Scientifique (CNRS), coordinated by GENCI (Grand Equipement National de Calcul Intensif) Grant 2022 A0122B06721. L.K. acknowledges with gratitude P. Dossin, H. Hu and Z. Alam for the warm hospitality at Procter and Gamble where this study has been initiated. O.K.M. also acknowledges funding from PETRONAS and the Royal Academy of Engineering for a Research Chair in Multiphase Fluid Dynamics, and the PETRONAS Centre for Engineering of Multiphase Systems. Simulations have been performed using code BLUE (Shin et al., 2017) and the visualisations have been generated using Paraview.

**Funding Statement.** This work is supported by the Engineering and Physical Sciences Research Council, United Kingdom, through the MEMPHIS (EP/K003976/1) and PREMIERE (EP/T000414/1) Programme Grants, and by computing time at HPC facilities provided by the Research Computing Service (RCS) of Imperial College London.

**Declaration of Interests.** The authors declare no conflict of interest.

**Author Contributions.** All authors have contributed equally to this paper.

**Data Availability Statement.** Raw data are available from the corresponding author L.K.

**Ethical Standards.** The research meets all ethical guidelines, including adherence to the legal requirements of the study country.

## References

- Aloi, L.E., & Cherry, R.S. (1996). Cellular response to agitation characterized by energy dissipation at the impeller tip. *Chemical Engineering Science*, *51*(9), 1523–1529.
- Ameur, H., Sahel, D., & Kamla, Y. (2017). Energy efficiency of a deep hollow bladed impeller for mixing viscoplastic fluids in a cylindrical vessel. *Advances in Mechanical Engineering*, *9*(5), 1687814016687912.
- Batels, C., Breuer, M., Wechdler, K., & Durst, F. (2020). Computational fluid dynamics applications on parallel-vector computer: Computations of stirred vessel flows. *Computer and Fluids*, *31*, 69–97.
- Beckett, C. (2006). *Thatcher*. Haus Publishing.
- Brucato, A., Ciofalo, M., Grisafi, F., & Micale, G. (1998). Numerical prediction of flow fields in baffled stirred vessels: A comparison of alternative modelling approaches. *Chemical Engineering Science*, *53*(21), 3653–3684.
- Busciglio, A., Caputo, G., & Scargiali, F. (2013). Free-surface shape in unbaffled stirred vessels: Experimental study via digital image analysis. *Chemical Engineering Science*, *104*, 868–880.
- Busciglio, A., Grisafi, F., Scargiali, F., & Brucato, A. (2014). Mixing dynamics in uncovered unbaffled stirred tanks. *Chemical Engineering Journal*, *254*, 210–219.
- Busciglio, A., Scargiali, F., Grisafi, F., & Brucato, A. (2016). Oscillation dynamics of free vortex surface in uncovered unbaffled stirred vessels. *Chemical Engineering Journal*, *285*, 477–486.
- Chisti, Y. (2000). Animal-cell damage in sparged bioreactors. *Trends in Biotechnology*, *18*(10), 420–432.
- Ciofalo, M., Brucato, A., Grisafi, F., & Torraca, N. (1996). Turbulent flow in closed and free-surface unbaffled tanks stirred by radial impellers. *Chemical Engineering Science*, *51*(14), 3557–3573.
- Daube, O. (1991). Numerical simulation of axisymmetric vortex breakdown in a closed cylinder. *American Mathematical Society*, *28*, 131–152.
- Dearhoff, J.W. (1970). A numerical study of three-dimensional turbulent channel flow at large Reynolds numbers. *Journal of Fluid Mechanics*, *41*, 453–480.

- Deshpande, S.S., Kar, K.K., Walker, J., Pressler, J., & Su, W. (2017). An experimental and computational investigation of vortex formation in an unbaffled stirred tank. *Chemical Engineering Science*, *168*, 495–506.
- Douglas Goff, H. (1997). Colloidal aspects of ice cream - a review. *International Dairy Journal*, *7*, 363–373.
- Fadlun, E.A., Verzicco, R., Orlandi, P., & Mohd-Yusof, J. (2000). Combined immersed-boundary finite-difference methods for three-dimensional complex flow simulations. *Journal of Computational Physics*, *161*, 35–60.
- Glover, G.C., & Fitzpatrick, J.J. (2007). Modelling vortex formation in an unbaffled stirred tank reactors. *Chemical Engineering Journal*, *127*(1–3), 11–22.
- Guadarrama-Pérez, R., Márquez-Baños, V.E., De La Concha-Gomez, A.D., Valencia-López, J.J., Vengoechea-Pimienta, A., Martínez de Jesús, G., & Ramírez-Muñoz, J. (2020). Hydrodynamic performance of a ring-style high-shear impeller in Newtonian and shear-thinning fluids. *Chemical Engineering and Technology*, *43*(11), 2325–2335.
- Hakansson, A. (2019). Emulsion formation by homogenization: Current understanding and future perspectives. *Annual Review of Food Science and Technology*, *10*, 239–258.
- Harlow, F.H., & Welch, J.E. (1965). Numerical calculation of time dependent viscous incompressible flow of fluid with free surface. *Physics of Fluids*, *8*, 2182–2189.
- Jansson, T.R.N., Haspang, M.P., Jesen, K.H., Hersen, P., & Bohr, T. (2006). Polygons on a rotating fluid surface. *Physical Review Letters*, *96*(4), 174502.
- Kahouadji, L. (2011). *Linear stability analysis for free surface rotating flow* (PhD thesis). Université Pierre and Marie Curie - Paris VI.
- Kahouadji, L., & Martin Witkowski, L. (2014). Free surface due to a flow driven by a rotating disk inside a cylindrical tank: Axisymmetric configuration. *Physics of Fluids*, *26*, 072105.
- Kahouadji, L., Nowak, E., Kovalchuk, N., Chergui, J., Juric, D., Shin, S., . . . Matar, O.K. (2018). Simulation of immiscible liquid-liquid flows in complex micro-channel geometries using a front-tracking scheme. *Microfluidics and Nanofluidics*, *22*, 126.
- Kwak, D.Y., & Lee, J.S. (2004). Multigrid algorithm for the cell-centred finite difference method II: Discontinuous coefficient case. *Numerical Methods for Partial Differential Equations*, *20*(5), 742–764.
- Lamberto, D.J., Alvarez, M.M., & Muzzio, F.J. (1999). Experimental and computational investigation of the laminar flow structure in a stirred tank. *Chemical Engineering Science*, *54*(7), 919–942.
- Lauder, B.E., & Spalding, D.B. (1974). The numerical computation of turbulent flows. *Computer Methods in Applied Mechanics and Engineering*, *3*, 260–289.
- Li, L., Wang, J., Feng, L., & Gu, X. (2017). Computational fluid dynamics simulation of hydrodynamics in an uncovered unbaffled tank agitated by pitched blade turbines. *Korean Journal of Chemical Engineering*, *34*(11), 2811–2822.
- Li, L., Xiang, K., & Xiang, B. (2020). Numerical simulation of transient power consumption characteristics in an unbaffled stirred tank. *Chemical Papers*, *74*(9), 2849–2859.
- Lilly, D.K. (1966a). *On the application of the eddy-viscosity concept in the inertial sub-range of turbulence* (Tech. Rep. 123). NCAR.
- Lilly, D.K. (1966b). The representation of small-scale turbulence in numerical simulation experiments. In *Proceedings of the IBM Scientific Computing Symposium on Environmental Sciences*. White Plains, NY: IBM Data Processing Division.
- Lopez, J.M. (1995). Unsteady swirling flow in an enclosed cylinder with reflectional symmetry. *Physics of Fluids*, *7*, 2700–2714.
- Martínez-de Jesús, G., Ramírez-Muñoz, J., García-Cortés, D., & Cota, L.G. (2018). Computational fluid dynamics study of flow induced by a grooved high-shear impeller in an unbaffled tank. *Chemical Engineering and Technology*, *41*(3), 580–589.
- McClements, D.J. (2004). *Food emulsions: Principles, practices, and techniques* (2nd ed.). Boca Raton, FL: CRC Press.
- Mc Millan, O.J., & Ferziger, J.H. (1979). Direct testing of subgrid-scale models. *AIAA Journal*, *17*, 1340–1346.
- Meyers, J., & Sagaut, P. (2006). On the model coefficients for the standard and the variational multi-scale Smagorinsky model. *Journal of Fluid Mechanics*, *569*, 287–319.
- Mohd-Yusof, J. (1997). Combined immersed-boundary/b-spline methods for simulations of flow in complex geometries. In *Center for Turbulence Research Annual Research Briefs* (pp. 317–327). Boca Raton, FL: CRC Press.
- Peskin, C.S. (1977). Numerical analysis of blood flow in the heart. *Journal of Computational Physics*, *25*, 220–252.
- Piva, M., & Meiburg, E. (2005). Steady axisymmetric flow in an open cylindrical container with a partially rotating bottom wall. *Physics of Fluids*, *17*, 063603.
- Poncet, S. (2005). *Écoulements de type rotor-stator soumis à un flux axial: De batchelor à stewartson* (PhD thesis). Université de Provence Aix-Marseille I.
- Pope, S.B. (2000). *Turbulent flows*. Cambridge, UK: Cambridge University Press.
- Pope, S.B. (2004). Ten questions concerning the large-eddy simulation of turbulent flows. *New Journal of Physics*, *6*, 35.
- Rao, A.R., & Kumar, B. (2007). The use of circular surface aerators in wastewater treatment tanks. *Journal of Chemical Technology and Biotechnology*, *82*(1), 101–107.
- Saad, Y. (2003). *Iterative methods for sparse linear systems* (2nd ed.). Philadelphia, PA: Society for Industrial and Applied Mathematics.
- Shin, S. (2007). Computation of the curvature field in numerical simulation of multiphase flow. *Journal of Computational Physics*, *222*, 872–878.
- Shin, S., Chergui, J., & Juric, D. (2017). A solver for massively parallel direct numerical simulation of three-dimensional multiphase flows. *Journal of Mechanical Science and Technology*, *31*, 1739.



- Shin, S., Chergui, J., Juric, D., Kahouadji, L., Matar, O.K., & Craster, R.V. (2018). A hybrid interface tracking-level set technique for multiphase flow with soluble surfactant. *Journal of Computational Physics*, *359*, 409–435.
- Shin, S., & Juric, D. (2009). A hybrid interface method for three-dimensional multiphase flows based on front tracking and level set techniques. *International Journal for Numerical Methods in Fluids*, *60*, 753–778.
- Smagorinsky, J. (1963). General circulation experiments with the primitive equations. I. The basic experiment. *Monthly Weather Review*, *91*, 99–164.
- Soligo, G., Roccon, A., & Soldati, A. (2020). Effect of surfactant-laden droplets on turbulent flow topology. *Physical Review Fluids*, *5*, 073606.
- Spohn, A. (1991). *Écoulement et éclatement tourbillonnaire engendré par un disque tournant dans une enceinte cylindrique* (PhD thesis). Université de Grenoble I.
- Spohn, A., Mory, M., & Hopfinger, E. (1993). Observations of vortex breakdown in an open cylindrical container with a rotating bottom. *Experiments in Fluids*, *14*, 70–77.
- Spohn, A., Mory, M., & Hopfinger, E. (1998). Experiments on vortex breakdown in a confined flow generated by a rotating disc. *Journal of Fluid Mechanics*, *370*, 73–99.
- Stewartson, K. (1953). On the flow between two rotating coaxial disks. *Mathematical Proceedings of the Cambridge Philosophical Society*, *49*(9), 333–341.
- Suzuki, T., Iima, M., & Hayase, Y. (2006). Surface switching of rotating fluid in a cylinder. *Physics of Fluids*, *18*, 101701.
- Vatistas, G.H. (1990). A note on liquid vortex sloshing and Kelvin's equilibria. *Journal of Fluid Mechanics*, *217*, 241–248.
- Vatistas, G.H., Wang, J., & Lin, S. (1992). Experiments on waves induced in the hollow core vortices. *Experiments in Fluids*, *13*, 377–385.
- Witz, C., Treffer, D., Hardiman, T., & Khinast, J. (2016). Local gas holdup simulation and validation of industrial-scale aerated bioreactors. *Chemical Engineering Science*, *152*, 636–648.